Aligned carbon nanotubes as polarization-sensitive, molecular near-field detectors

Ertugrul Cubukcu[a,1], Fatih Degirmenci[a], Coskun Kocabas[b], Mariano A. Zimmler[a], John A. Rogers[c], and Federico Capasso[a,1]

[a]School of Engineering and Applied Sciences, Harvard University, 9 Oxford Street, Cambridge, MA 02138; [b]Department of Chemistry and Chemical Biology, Harvard University, 12 Oxford Street, Cambridge, MA 02138; and [c]Department of Materials Science and Engineering, University of Illinois, Urbana, IL 61801

Contributed by Federico Capasso, December 31, 2008 (sent for review November 9, 2008)

Near-field scanning optical microscopes are widely used in imaging of subwavelength features in various material systems and nanostructures. For a variety of applications, polarization-sensitive near-field probes can provide valuable information on the nature and symmetry of the imaged nanoparticles and emitters. Conventional near-field optical microscopy lacks in-plane polarization sensitivity. Here, we use aligned single-wall carbon nanotubes as polarization-sensitive molecular scale probes to image the transverse near-field components of an optical Hertzian dipole antenna. Because of the Raman ''antenna effect'' in carbon nanotubes, only the near-field components along the nanotube axis are detected. These findings demonstrate that aligned carbon nanotubes can be used as polarization-sensitive near-field detectors.

optical antenna | plasmonics

Optical antennas (1–4) are the analogs for light of radio frequency dipole antennas. Recently, they have been of scientific and technological interest for their ability to enhance and localize electromagnetic radiation (5–11). A gold or silver nanoparticle of any shape, e.g., a nanosphere, a nanorod, or a nanoprism, serves as an optical antenna owing to the oscillation of the conduction electron plasma (Mie resonances) (12, 13). The near fields generated by metallic nanostructures offer some intriguing features such as polarization control of single-molecule emission (14, 15). A polarization-sensitive nanoscale probe that does not perturb the near fields generated by optical antennas would be invaluable for studying these features. To this end, we have explored the properties of aligned single-walled carbon nanotubes (SWCNTs) (16), quasi-1-dimensional macromolecules that are formed by rolled-up single graphene sheets.

Depending on their chirality, SWCNTs can be either metallic or semiconducting (17). Both varieties, however, exhibit Van Hove singularities in their electronic band structures, allowing for resonant absorption and scattering of light (18). Resonant Raman (19) and Rayleigh (20) spectroscopic studies of single SWCNTs have demonstrated the strong polarization-dependence of these phenomena. Optical absorption of SWCNTs is strongly suppressed when the polarization of light is perpendicular to the nanotube axis (20, 21). This suppression is attributed to the depolarization effect (21), i.e., the ''antenna effect'' (22, 23). A parallel external field will induce charges only at the extremities of the SWCNT similar to an antenna, whereas a perpendicular field would induce charges in the SWCNT walls that would, in turn, cancel the external field.

Because Raman scattering from SWCNTs depends on the polarization of the exciting field, SWCNTs can be used as polarization-dependent nanoscopic near-field ''detectors.'' With this approach, we have directly imaged the distribution of transverse near fields generated by gold nanodisk antenna arrays via surface-enhanced Raman scattering (SERS) from the SWCNTs with the excitation laser polarization perpendicular to them (Fig. 1*A*). Using SWCNTs as Raman antennas requires perfectly aligned SWCNT arrays because this would cause all of the SWCNTs to respond in concert to a particular polarization determined by the alignment direction. Recent advances in SWCNT synthesis (24, 25) allow us to realize the proposed idea.

Fig. 1 *B* and *C* shows the calculated local field generated along the x axis around a gold nanodisk antenna upon illumination by a plane wave polarized along the x and y directions, respectively. A commercial finite integration technique (FIT) code (CST Microwave Studio) is used for solving the 3-dimensional antenna problem. The nanoantenna array on a quartz substrate is illuminated with a plane wave of wavelength 633 nm propagating in the z-direction. In the near zone of the nanodisk antenna, all 3 electric field components exist, as it would be for any dipole. For a subwavelength dipole the near zone electric field is given as

$$\vec{E} = (3\vec{p}(\vec{n}\cdot\vec{p}) - \vec{p})/r^3, \quad [1]$$

where $\vec{n}$ is the unit vector along r, the radial distance from the dipole (26). For a dipole moment $\vec{p}$ along the x axis, Eq. **1** has all x, y, and z components. Because our nanodisk antenna is much smaller than the wavelength of the incident light, it can be treated as a Hertzian dipole, which has the near-field distribution given by Eq. **1**. The in-plane parallel x component and transverse y component of the near fields generated by the antenna array are comparable in strength (Fig. 1). To image these 2 different polarization components, one needs a polarization-sensitive near-field ''detector'' that would not perturb the near fields of the nanodisk antenna. Here, we propose and demonstrate the use of aligned SWCNTs as near-field probes. Fig. *1D* shows a scanning electron microscope (SEM) image of a typical structure that comprises gold nanodisks fabricated around aligned SWCNTs.

Aligned single-wall SWCNT arrays are grown on single crystal quartz wafers by using a chemical vapor deposition technique (24, 25). A photolithographically patterned thin Fe film (<0.2 nm) is used as a catalyst. The growth was performed at 925 °C at atmospheric pressure. Carrier gases, Ar (10 sccm) and H_2 (10 sccm), flow into the chamber through an ethanol bubbler. After 20 min, the growth process is terminated. The average diameter and the length of the SWCNTs grown by this process are 1.5 nm and 100 μm, respectively (Fig. S1).

We fabricate the gold nanodisk arrays by a standard bilayer e-beam lithography process. First 2 layers of e-beam resist are

Author contributions: E.C. designed research; E.C., F.D., C.K., M.A.Z., J.A.R., and F.C. performed research; E.C. and F.D. analyzed data; and E.C., J.A.R., and F.C. wrote the paper.

The authors declare no conflict of interest.

Freely available online through the PNAS open access option.

[1]To whom correspondence may be addressed. E-mail: cubukcu@post.harvard.edu or capasso@seas.harvard.edu.

This article contains supporting information online at www.pnas.org/cgi/content/full/0812217106/DCSupplemental.

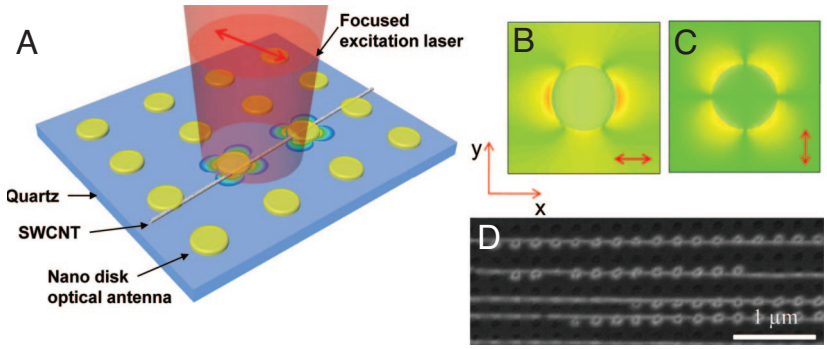

Fig. 1. Schematic representation of the polarization-sensitive SWCNT near-field detector configuration. (*A*) Shown is a schematic of the spatial distribution in the vicinity of the metallic nanodisks of the near-field amplitude along the *x* direction, when the laser is polarized normal to the SWCNT. (*B* and *C*) Calculated near-field amplitude distribution along the *x* direction generated around a single nanodisk optical antenna in a square array for illumination polarized parallel (*B*) and perpendicular (*C*) to the SWCNT assumed oriented along the *x* direction. The nanodisk thickness, the nanodisk diameter, and the period of the array are 35, 130, and 300 nm, respectively. The red arrow shows the polarization of the incident plane wave. The color scale is the same for both *B* and *C*. (*D*) Exemplary SEM image of the coupled system of the aligned SWCNT antennas and the gold nanodisk antenna array.

spincast on the substrate, followed by a 5-nm-thick Cr evaporation to avoid charging during e-beam writing. After the removal of the Cr layer and development of the resist, 35 nm of Au is evaporated after a 3-nm Ti adhesion layer. Then the nanodisks are revealed with a lift-off process. Arrays are fabricated both in periodic and quasiperiodic Penrose lattice arrangements (*SI Text* and Fig. S2] (27). Atomic force microscope (AFM) image of the fabricated square array structure is shown in Fig. 2*A*. The good alignment between the nanodisk antennas and the SWCNTs is visible in Fig. 2*A*. The nanodisks in these arrays have a diameter of 130 ± 10 nm (Fig. 2*B*) and the array period is chosen to be 300 nm.

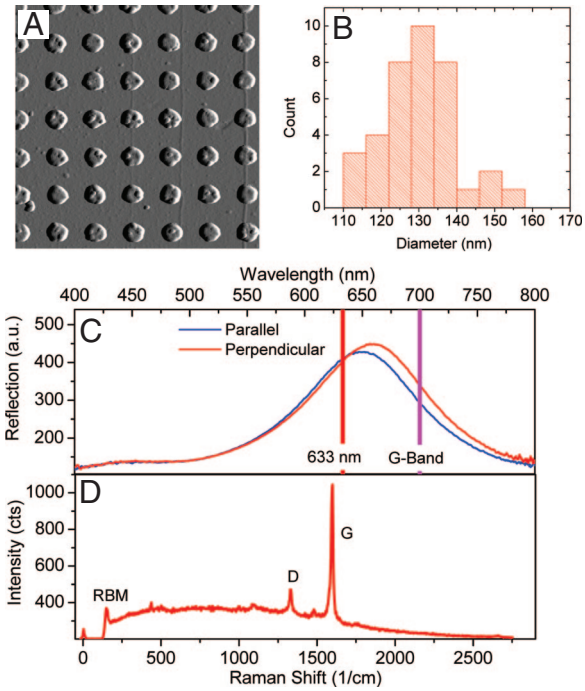

Fig. 2. Experimental characterization of coupled SWCNT and nanodisk arrays. (*A*) AFM image of the square antenna array. Alignment between the SWCNTs along the symmetry direction of the square nanodisk array is visible. The scan area is 2 × 2 μm. (*B*) Histogram showing the diameter distribution for the fabricated nanodisks in the square array. (*C*) Localized plasmon resonance spectrum of the antenna array for polarizations parallel (blue) and perpendicular (red) to the SWCNTs. The excitation (633 nm) and the Raman (G-band) lines are represented as vertical lines. (*D*) Exemplary SERS spectrum of a SWCNT coupled to the nanodisk array. The radial breathing mode (RBM), the D-band, and G-band Raman lines are labeled. Note the hump-shaped fluorescent background from the gold nanodisks.

We characterized the localized surface plasmon resonances of our 100-μm × 100-μm nanoantenna arrays by far-field reflection measurements (28). An incoherent white light source is collimated and then sent through a broadband polarizer and a long-working-distance, N.A. 0.55, microscope objective onto the arrays. The reflected light is then collected back through the same objective and fiber-coupled into a spectrometer. Each spectrum is corrected for the background and the wavelength dependence of the light source by normalizing to the reflection of the quartz substrate itself. Fig. 2*C* shows the reflection spectrum of the square nanodisk array for polarizations parallel and perpendicular to the axes of the SWCNTs. The resonance wavelengths for the nanodisk arrays do not change significantly with the polarization. Note that we have chosen array parameters such that the plasmonic resonance wavelength lies between the laser excitation line and the G-band Raman line (Fig. 2*C*).

We use a sample scanning confocal optical microscope fiber-coupled to a sensitive spectrometer for Raman measurements of the SWCNTs. The 633-nm line of a He–Ne laser is expanded and sent through a holographic laser line cleanup filter and focused on to the sample by a 0.9 N.A. 100× objective. Reflected light is collected back through a long-pass filter to suppress the excitation beam. A representative surface-enhanced resonant SWCNT Raman spectrum from the square array for laser polarization parallel to the SWCNT is shown in Fig. 2*D*. The radial breathing mode (RBM), the defect induced mode (D) and the tangential stretching mode (G) are all identified (21). The hump-shaped background is due to the photoluminescence from the gold nanoantennas (29).

The SEM image in Fig. 3*A* corresponds to the edge of the square antenna array. We have performed confocal Raman microscopy (CRM) on this region because it allows us to distinguish the antenna enhanced and regular Raman emission from individual resonant SWCNTs. The Raman spectrum is collected at every pixel for 500 ms by moving the scan stage in 200-nm steps in a 20-μm × 20-μm area. The laser power at the objective focus was kept at ≈800 μW to avoid melting of the gold nanodisks. Fig. 3*B* shows the Raman enhancement along the same SWCNT corresponding to the black vertical dashed lines in Fig. 3 *C* and *D*. Clearly, there is nanodisk enhanced Raman scattering for both polarizations. Fig. 3*C* is then generated by integrating the G-band Raman intensity for the parallel polar-

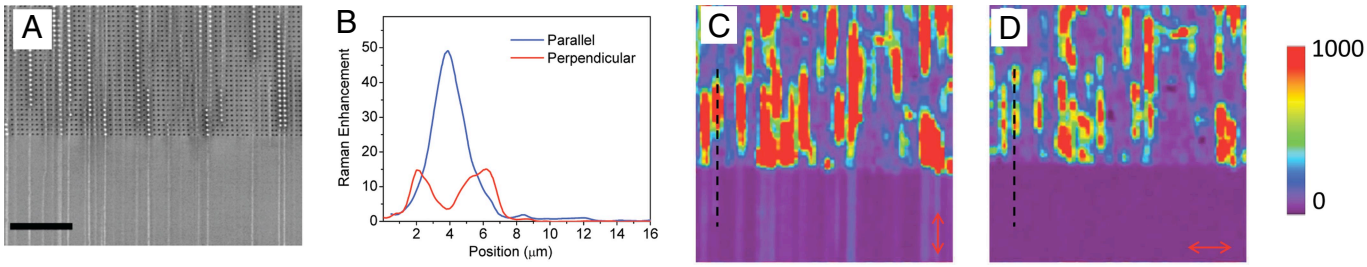

Fig. 3. Confocal Raman imaging of nanodisk arrays. (*A*) SEM image of the area in the square array that is investigated with confocal Raman microscopy in *C* and *D*. The nanodisks touching SWCNTs appear brighter because of the charging contrast in SEM imaging. These brighter regions also correspond to the ''hot spots'' that generate the strongest coupling between the SWCNT antennas and the nanodisks in turn causing surface enhanced Raman scattering. (Scale bar: 4 μm.) (*B*) The Raman intensity enhancement for parallel (red) and perpendicular (blue) polarizations along the black vertical dashed line in *C* and *D*, respectively. This shows how the enhancement factor changes along the same SWCNT for different polarizations. The enhancement is calculated by dividing the antenna enhanced Raman intensity by the Raman intensity from the pristine SWCNT. (*C*) Confocal Raman microscope (CRM) image of a 20-μm $\times$ 20-μm area with the laser polarization along the SWCNTs. This image is generated by spectrally integrating the intensity in the G-band for every pixel. G-band emission from SWCNTs that are not in contact with the gold nanodisks is visible for this polarization because of the ''SWCNT antenna'' effect. Surface enhanced Raman scattering is driven by the near-field distribution shown in Fig. 1*B*. (*D*) Same as *C* for perpendicular laser polarization. No Raman scattering from pristine SWCNTs is observed. For this case, surface-enhanced Raman scattering is driven by the transverse near-field component shown in Fig. 1*C*.

ization and subtracting the gold fluorescence at every pixel. Note that only the nanotubes absorbing at the excitation wavelength are visible in the Raman image. For this polarization, SWCNTs generate G-band Raman signal even without the coupling to the gold nanodisk antennas. In the bottom part of the region shown in Fig. 3*C*, the ''pristine'' SWCNTs are visible as straight vertical lines with their widths defined by the diffraction limited optical spot of the excitation laser. When the laser polarization is along the SWCNTs, the G-band Raman is excited by the parallel component (Fig. 1*B*) of the nanodisk near field and is enhanced.

Fig. 3*D* shows the Raman intensity map of the same region with the laser polarization perpendicular to the SWCNT alignment direction. There is Raman signal only from the SWCNTs driven by the transverse in-plane component of the near fields that are generated around the nanodisk antennas by the cross-polarized incident laser. This transverse component (Fig. 1*C*) is parallel to the SWCNTs and thus leads to Raman scattering. The polarization dependence of G-band signal allows us to distinguish the enhancements due to the 2 polarizations generated by the nanodisk, which are comparable in field strength as shown by our electromagnetic simulations (Fig. 1).

In the regions where the resonant SWCNTs interact with the nanodisks, there is surface enhancement in the Raman scattering. Although the SWCNTs extend spatially across the region that was imaged, not the entire SWCNT necessarily interacts with a chain of nanodisks because of a slight misalignment between the SWCNTs and the nanodisk array. This is seen in Fig. 3*A* for the square array where the nanoantennas touching the SWCNTs appear brighter because of a charging contrast in the SEM imaging (30).

The measured enhancements ($\approx$20) are many orders of magnitude smaller than those achieved with metallic structures used for single-molecule Raman spectroscopy (31, 32). For single-molecule studies, Raman signals originate from molecules adsorbed on random sites on the metallic nanoparticles involved. One should bear in mind that a 2-nm gold nanosphere, comparable in size, with typical surface roughness, exhibits Mie resonances; thus a small-scale roughness or a sharp edge on the metallic particle will strongly perturb the local near fields, yielding large near-field enhancements while leaving the far-field response intact. If the molecule at hand is small, then it can land on any of these random ''hot spots'' on the nanostructure. In our case, we are dealing with SWCNTs that are macromolecules with well-defined orientations that extend across the nanodisks, causing the Raman response to be averaged out spatially over the nanoantennas. Another factor reducing the enhancement is the distance between the nanoantennas and the molecule of interest. Unlike fluorescence, Raman scattering is not quenched at short distances from metals and decreases with increasing distance. In our configuration, there is a 3-nm Ti adhesion layer acting as an optically lossy spacer between the SWCNTs and the gold nanodisks, whereas in single-molecule studies, there is a physical contact with the gold nanoparticles.

We have thus far demonstrated that SWCNTs can be used to detect different polarization components of dipole near fields. The question to ask now is whether we can also extract some information on the spatial distributions or symmetries of these near fields. In conventional near-field microscopy (33), a probe is scanned over the optical near-field distribution of interest to map out the spatial extent of the former. In our configuration, both the probe (the SWCNT detector) and the object (the nanodisk antenna) are fixed on the quartz substrate. At first glance, it seems impractical to change the distance between the probe and the object. Nonetheless, the nanodisks are identical, and there is a slight misalignment between the SWCNTs and the nanodisk arrays. If we can find a SWCNT that crosses from one side of a row of nanodisks to the other (Fig. S3), we will have a distribution of lateral distances between the probe and the nanodisks. The aforementioned SEM imaging contrast aids us in finding such a SWCNT. Then by correlating the SEM images with the CRM images for different polarizations, we can retrieve spatial information on the near fields generated by the nanoantennas. Yet another caveat is that the whole section of the SWCNT lying in the confocal volume will contribute to the Raman signal, causing the latter to be spatially averaged.

To emulate the experimental situation, we have used the configuration shown in Fig. 4*A*. Because the SERS signal is approximately proportional to the fourth power of the near-field enhancement (33), we model the SWCNT as a detector that averages $|E|^4$ over its length along the x direction. We then calculate the line-averaged field enhancement $\langle|E|^4\rangle$ as a function of the distance Δy between the SWCNT detector and the nanodisk center. Fig. 4 *B* and *C* shows the $\langle|E\rangle^4\rangle$ for parallel and perpendicular polarizations, respectively. Although our approach does not provide a 2-dimensional map of the near-field distribution, it nevertheless distinguishes the 2 distinct symmetries associated with the polarization components.

An SEM image of a SWCNT that crosses 18 nanodisks is shown in Fig. 4*D*. The bright nanodisks are the indication of the physical contact between the SWCNT and the gold nanoantennas. The SWCNT touches the far-right bright nanodisk on the

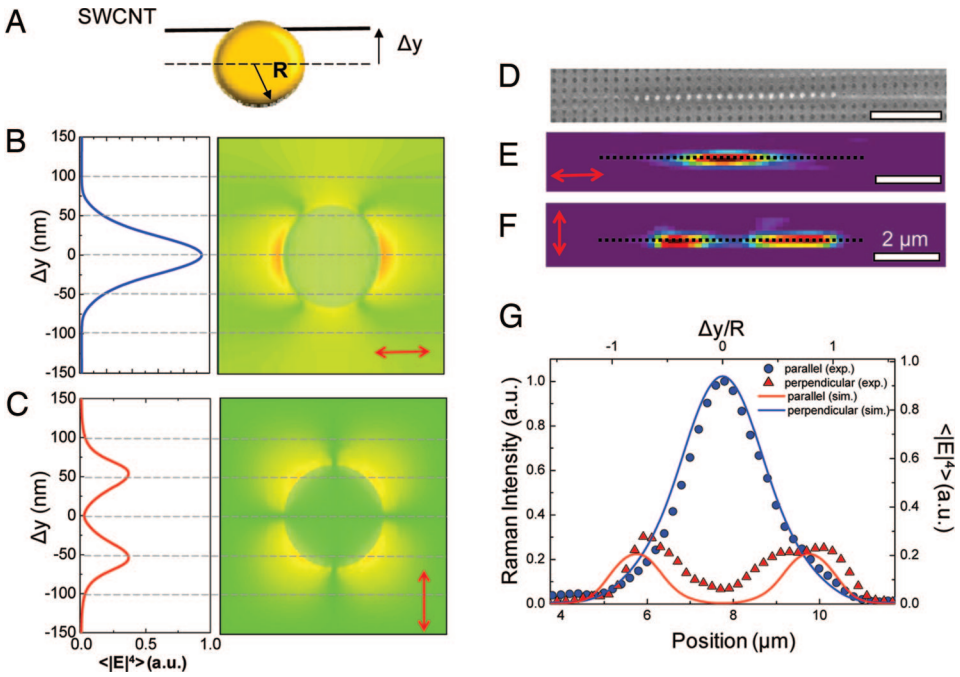

Fig. 4. Near field imaging of the nanodisk array with a SWCNT. (*A*) Schematic of SWCNT detector probing the local field around a nanodisk. R and Δy are the nanodisk radius and the distance between the SWCNT and the nanodisk center, respectively. (*B*) Calculated normalized average $|E|^4$ distribution along the *y* axis for parallel laser polarization. $\langle|E|^4\rangle$ denotes spatial averaging along the *x* axis. Note that measured Raman signal averaged over the SWCNT is proportional to $\langle|E|^4\rangle$. (*C*) Same as *B* for perpendicular polarization. (*D*) SEM image of a representative SWCNT coupled to a row of nanodisks. Nanodisks touching the SWCNT appear brighter. (Scale bar: 2 μm.) (*E* and *F*) CRM image of the SWCNT in *D* for parallel (*E*) and perpendicular (*F*) laser polarization. Arrows show the laser polarization. (*G*) Comparison between simulations and CRM measurements. The solid lines are the simulation results from *B* and *C* for parallel (blue) and perpendicular (red) illuminations. Measured Raman intensity distributions along the SWCNT in *D* for parallel (blue circles) and perpendicular (red triangles) laser polarizations, along the black dotted lines in *E* and *F*, respectively. Note that because of the misalignment between a particular SWCNT and the row of nanodisks, each $\Delta y/R$ (upper horizontal axis) corresponds to a different position along the nanotube (lower horizontal axis).

bottom edge of the nanodisk and goes across the row of 18 nanodisks ending its physical contact at the top edge of the leftmost bright nanodisk. The CRM images corresponding to this region are shown in Fig. 4 *E* and *F* for parallel and perpendicular laser polarizations, respectively. Fig. 4*G* compares the experimental results with the simulations. There is good qualitative agreement between the theory and the experiment. The symmetries associated with different polarizations are deduced by using our approach. The ratio of the measured field enhancements for the 2 polarizations is also consistent with the calculated values.

In summary, we have demonstrated both experimentally and theoretically that aligned SWCNTs can be used as polarization-sensitive near-field probes to image, by far-field microscopy techniques, the different polarization components generated by optical dipole nanoantennas. This work, which combines metallic nanoparticles and SWCNTs is likely to open up vistas in nanophotonics and plasmonics.

ACKNOWLEDGMENTS. This work was supported by the Air Force Office of Scientific Research under Contract No. FA9550-05-1-0435 and by Defense Advanced Research Projects Agency (Center for Micromechanical and Plasmonic Systems) under Contract No. HR0011-06-1-0044.

1. Muhlschlegel P, Eisler HJ, Martin OJF, Hecht B, Pohl DW (2005) Resonant optical antennas. *Science* 308:1607–1609.
2. Schuck PJ, Fromm DP, Sundaramurthy A, Kino GS, Moerner WE (2005) Improving the mismatch between light and nanoscale objects with gold bowtie nanoantennas. *Phys Rev Lett* 94:017402.
3. Crozier KB, Sundaramurthy A, Kino GS, Quate CF (2003) Optical antennas: Resonators for local field enhancement. *J Appl Phys* 94:7950.
4. Novotny L (2007) Effective wavelength scaling for optical antennas. *Phys Rev Lett* 98:266802.
5. Farahani JN, Pohl DW, Eisler HJ, Hecht B (2005) Single quantum dot coupled to a scanning optical antenna: A tunable superemitter. *Phys Rev Lett* 95:017402.
6. Bharadwaj P, Anger P, Novotny L (2007) Nanoplasmonic enhancement of single-molecule fluorescence. *Nanotechnology* 18:044017.
7. Anger P, Bharadwaj P, Novotny L (2006) Enhancement and quenching of single-molecule fluorescence. *Phys Rev Lett* 96:113002.
8. Cubukcu E, Kort EA, Crozier KB, Capasso F (2006) Plasmonic laser antenna. *Appl Phys Lett* 89:093120.
9. Gonzalez FJ, Ilic B, Alda J, Boreman GD (2005) Antenna-coupled infrared detectors for imaging applications. *IEEE J Sel Top Quantum Electron* 11:117–120.
10. Alu A, Engheta N (2008) Tuning the scattering response of optical nanoantennas with nanocircuit loads. *Nat Photonics* 2:307.
11. Alu A, Engheta N (2008) Input impedance, nanocircuit loading, and radiation tuning of optical nanoantennas. *Phys Rev Lett* 101:043901.
12. Bohren CF, Huffman DR (1983) *Absorption and Scattering of Light by Small Particles*. (Wiley Interscience, New York).
13. Kelly KL, Coronado E, Zhao LL, Schatz GC (2003) The optical properties of metal nanoparticles: The influence of size, shape, and dielectric environment. *J Phys Chem B* 107:668–677.
14. Gersen H, *et al.* (2000) Influencing the angular emission of a single molecule. *Phys Rev Lett* 85:5312–5315.
15. Moerland RJ, Taminiau T, Novotny L, Van Hulst NF, Kuipers L (2008) Reversible polarization control of single photon emission. *Nano Lett* 8:606–610.
16. Reich S, Thomsen C, Maultzsch J (2004) *Carbon Nanotubes: Basic Concepts and Physical Properties*. (Wiley-VCH, Weinheim, Germany).
17. Jorio A, *et al.* (2001) Structural (n, m) determination of isolated single-wall carbon nanotubes by resonant Raman scattering. *Phys Rev Lett* 86:1118–1121.
18. Jorio A, *et al.* (2000) Polarized Raman study of single-wall semiconducting carbon nanotubes. *Phys Rev Lett* 85:2617–2620.
19. Duesberg GS, Loa I, Burghard M, Syassen K, Roth S (2000) Polarized Raman spectroscopy on isolated single-wall carbon nanotubes. *Phys Rev Lett* 85:5436–5439.
20. Sfeir MY, *et al.* (2004) Probing electronic transitions in individual carbon nanotubes by Rayleigh scattering. *Science* 306:1540–1543.
21. Cardona M, Merlin R, eds (2007) *Light Scattering in Solids IX: Novel Materials and Techniques* (Springer, Berlin), Vol 108.
22. Wang Y, *et al.* (2004) Receiving and transmitting light-like radio waves: Antenna effect in arrays of aligned carbon nanotubes. *Appl Phys Lett* 85:2607–2609.

23. Kempa K, *et al.* (2007) Carbon nanotubes as optical antennae. *Adv Mat* 19:421–426.
24. Kocabas C, *et al.* (2005) Guided growth of large-scale, horizontally aligned arrays of single-walled carbon nanotubes and their use in thin-film transistors. *Small* 1:1110–1116.
25. Kocabas C, Shim M, Rogers JA (2006) Spatially selective guided growth of high-coverage arrays and random networks of single-walled carbon nanotubes and their integration into electronic devices. *J Am Chem Soc* 128:4540–4541.
26. Jackson JD (1998) *Classical Electrodynamics* (Wiley, New York), 3rd Ed.
27. Steinhardt PJ, Ostlund S (1987) *The Physics of Quasicrystals* (World Scientific, Teaneck NJ).
28. Smythe EJ, Cubukcu E, Capasso F (2007) Optical properties of surface plasmon resonances of coupled metallic nanorods. *Opt Express* 15:7439–7447.
29. Beversluis MR, Bouhelier A, Novotny L (2003) Continuum generation from single gold nanostructures through near-field mediated intraband transitions. *Phys Rev B* 68:115433.
30. Kumar R, Zhou H, Cronin SB (2007) Surface-enhanced Raman spectroscopy and correlated scanning electron microscopy of individual carbon nanotubes. *Appl Phys Lett* 91:223105.
31. Nie SM, Emery SR (1997) Probing single molecules and single nanoparticles by surface-enhanced Raman scattering. *Science* 275:1102–1106.
32. Kneipp K, *et al.* (1997) Single molecule detection using surface-enhanced Raman scattering (SERS). *Phys Rev Lett* 78:1667–1670.
33. Novotny L, Hecht B (2006) *Principles of Nano-Optics* (Cambridge Univ Press, Cambridge, UK).